Enhanced magnetostriction through dilute Ce doping of Fe-Ga

Alexander A. Baker,[*] Alfred Amon, Emily E. Moore, Hunter B. Henderson, Jibril Shittu, Connor J. Rietema, Aurelien Perron, and Scott K. McCall
Lawrence Livermore National Laboratory, Livermore, California 94550, USA

(Received 27 October 2022; accepted 1 December 2022; published 17 January 2023)

Doping of magnetostrictive galfenol ($Fe_{82}Ga_{18}$, in at. %) with rare-earth elements significantly enhances magnetostriction, with the largest gains achieved in textured melt-spun ribbons. Here, it is demonstrated that even extremely dilute Ce, as little as 65 ppm, can double the magnetostrictive response of galfenol when coupled with an appropriate heat treatment. This improvement is correlated with a compression of the host lattice, both of which reach their maximum extent at the calculated solubility limit of Ce in in body-centered cubic (bcc) galfenol, ~ 50 ppm. Beyond this point, excess Ce segregates into $CeGa_2$, which forms an interdendritic network throughout the sample at high Ce levels and cannot be resolutionized through heat treatments. These findings point to the importance of solubility limits (i.e., equilibrium thermodynamics) in determining appropriate doping levels or heat treatment couples to optimize magnetostrictive performance, confirming that overdoping is actively detrimental to both material properties and cost.

DOI: 10.1103/PhysRevMaterials.7.014406

I. INTRODUCTION

Magnetostrictive materials such as galfenol ($Fe_{82}Ga_{18}$) and Terfenol-D ($Tb_{0.3}Dy_{0.7}Fe_2$) display a magnetostructural coupling that leads to volume-conserving deformation under an applied magnetic field. Technologies that employ such magnetostrictive materials rely on the reversible exchange of magnetic and mechanical energy resulting in strain-induced deformation or, conversely, a stress-induced change in magnetic permeability. The versatility in response of these materials to external forces make them useful across a range of industrial applications, including high-precision actuators, sensors, and potentially tunable inductors [1,2]. However, the presence of critical rare earths (REs) Tb and Dy in Terfenol-D makes it expensive and vulnerable to supply disruptions, necessitating the development of alternative, lower cost magnetostrictive materials that retain large relative length change λ under a magnetic field. Recently, it has been shown that doping REs into the body-centered cubic (bcc) lattice of Fe-Ga can lead to a significant increase in magnetostriction, with reports of values as high as 1500 ppm for 0.2 at. % La additions to melt-spun ribbons [3,4]. Authors of several studies have investigated ribbons with varying Ga content, $Fe_{100-x}Ga_xRE_{0.2}$ [3] and several different RE species with levels ranging from 500 to 4000 ppm [4–9]. They showed significant increase in magnetostriction because of RE doping, attributing the benefits to local solute strain induced within the disordered bcc A2 lattice. The gains that can be achieved are apparently limited by the solubility of the RE within the FeGa lattice, with further addition of RE leading to the formation of additional RE-Ga compounds rather than enhancing magnetostriction. Here, the melt spinning provides an extremely fast cooling rate that significantly increases the solubility of the RE due to the far-from-equilibrium process conditions.

In this paper, we investigate dilute concentrations of Ce, from 0 to 10 000 ppm, focusing particularly < 500 ppm to probe the effects of the solubility of Ce on the magnetostrictive properties of galfenol. Cerium should be a particularly effective dopant for enhancing magnetostriction due to its large negative quadrupole moment, as investigated by He *et al.* [3]. Our work is guided by thermodynamic calculations using the calculation of phase diagrams (CALPHAD) method, which permits prediction of phase stability and transitions across temperatures and compositions for multicomponent systems. This knowledge is used to improve the alloy composition and processing parameter (i.e., heat treatment) couple to avoid phases that might prove deleterious to enhancing magnetostriction such as $CeGa_2$. Samples are fabricated by arc melting then heat treated (homogenization into the single bcc phase domain) and quenched to conserve the predicted thermodynamic equilibrium. This approach produces polycrystalline samples without a preferred orientation, leading to a reduced magnetostriction compared with single crystals or the highly textured ribbons produced by melt spinning.

Experimentally, we find that the optimal doping level for Ce in $Fe_{81.7}Ga_{18.3}$ is as low as ~ 65 ppm, close to the solubility limit of Ce in $Fe_{81.7}Ga_{18.3}$, as above this level, $CeGa_2$ formation is preferred, and more Ce confers no additional benefit. By 675-ppm Ce, the addition of Ce is actively detrimental to magnetostrictive performance, as the formation of the $CeGa_2$ phase reduces observed volume change. Further, it cannot be removed easily using solutionizing heat treatments due to the extremely low solubility and mobility of Ce in Fe [10]. This finding is consistent with previous reports of nonequilibrium synthesis methods such as melt spinning, where maximum magnetostriction is reached at 0.05 to 0.2 at. % RE (corresponding to 500 and 2000 ppm, respectively)

---

[*] baker97@llnl.gov

[3,5,6,8]. Above this point, networks of $REGa_2$ intermetallics form, leading to reduced magnetostriction for overdoped samples.

II. EXPERIMENTAL

Iron shot (99.99%, Alfa Aesar), gallium ingot (99.99%, Alfa Aesar), and cerium rod (99.99%, Alfa Aesar) were arc melted with a target volume of 2 mL. Each sample was melted 4 times, flipping between melts to ensure homogeneity. Portions of the as-melted samples were heat treated at 1200° C for 4 h under flowing UHP Ar, followed by a water quench to reduce the $CeGa_2$ fraction. Samples were wrapped in Ta foil to minimize oxidation and suspended in a vertical tube furnace, then dropped into water upon completion of the heat treatment. Target Ce compositions were 0, 10, 50, 200, 1000, and 10 000 ppm. Cerium concentration in the cast alloys was determined by inductively coupled plasma mass spectrometry, after digestion of alloy pieces in 8M hydrochloric acid (Fisher, trace metal grade). Actual compositions of 0, 30, 65, 155, 675, and 10 260 ppm were found—measured numbers will be used to identify samples throughout this paper.

Magnetostriction measurements were performed using Omega strain gauges with large active areas (5×10 mm) mounted using M-bond 200 adhesive and standard surface preparation procedures. Samples were typically $15 \times 10 \times 1$ mm slabs, with the magnetic field constrained to lie within the plane of the sample to minimize demagnetization effects. Gauges were mounted such that the sensitivity axis of the strain gauge was perpendicular to the cooling direction (parallel to the hearth surface of the arc melter). Measurements were conducted in a Quantum Design Physical Properties Measurement System, with samples mounted on a rotating sample holder using GE varnish, such that the applied field was swept in the plane of the sample. The resistance of the strain gauge was measured using AC detection with a frequency of 17 Hz, and magnetostriction was calculated using the relative change in resistance and the gauge factor of the strain gauge (typically 2.06). Measurements were conducted at 300 K, either as a function of angle between strain gauge and a fixed field of 5 kOe, or as a function of applied field parallel and perpendicular to the sensing direction of the strain gauge [11]. The reported maximum magnetostriction represents the difference in magnetostriction between measurement with field parallel to the strain gauge and normal to the strain gauge. This eliminates errors due to an undefined initial magnetic domain distribution.

X-ray diffraction measurements were performed on polished slabs using a Bruker D8 diffractometer (Cu $K\alpha$ radiation, Ni filter) and a Lynxeye 1D detector. Significant background was observed due to secondary fluorescence from the Fe content.

X-ray absorption spectroscopy (XAS) and x-ray magnetic circular dichroism (XMCD) measurements were conducted at beamline 6.3.1 of the Advanced Light Source (Berkeley, California), using surface-sensitive total electron yield (TEY) mode at the Fe $L_{2,3}$ and Ce $M_{4,5}$ absorption edges. Samples were polished in an Ar glove box to remove surface oxide and transported to the beamline sealed under Ar to minimize surface oxidation. Samples were loaded into an ultra-high vacuum chamber in < 5 min; however, some evidence of oxidation was present at the Fe absorption edges. Spectra were acquired in flying scan mode with typical velocity of 1 eV/s, with a fixed negative polarization. A magnetic field of 4 kOe was applied parallel to the beam; this was flipped between scans to enable calculation of XMCD from the difference between sequential scans. Data were normalized to the incident beam intensity, collected immediately upstream of the measurement chamber, to correct for energy and time-dependent fluctuations. Then a linear background was fitted to the pre-edge region and subtracted. The step edge was scaled to 1 for XMCD sum-rule analysis.

Metallographic specimens were prepared with standard mount and polish methods. Scanning electron microscopy (SEM) micrographs were collected on a Thermo Fisher Apreo, primarily at 10 kV accelerating voltage and with the T1 in-lens detector. This detector primarily detects backscatter electrons, making Ce-rich regions appear bright while also providing some channeling contrast to distinguish areas with different crystallographic orientation. Electron backscatter diffraction (EBSD) provided information on the crystallographic morphology of the specimens. The samples were ground flat and polished to a 40-nm colloidal silica surface finish. The patterns were collected with a 20-kV accelerating voltage, 6.4-nA beam current, and 12-mm working distance. The step size for the scans was set to 3 μm. In postprocessing, EDAX OIM Analysis software was used to perform a neighbor confidence index (CI) correlation cleaning step (min CI 0.1, integration factor 0.05) altering 5% or fewer data points in the final dataset.

III. THERMODYNAMIC MODELING

Thermodynamic modeling provides guidance in finding a temperature-composition space where Ce solubility in bcc-(Fe-Ga) is maximized for optimal magnetostrictive properties. The CALPHAD method [12–14] is based on mathematical models that use adjustable parameters to describe Gibbs energies as a function of temperature and composition of various phases in each alloy system. These models are used to perform equilibrium calculations and predict phase stabilities for an efficient and effective method to design magnetostrictive materials. This paper is based on the extrapolation of three constituent binaries reported in Fig. 1: Fe-Ga [15], Fe-Ce [16], and Ce-Ga [17].

The Fe-Ga system is modeled using four stoichiometric phases– – Fe_3Ga, $Fe_6Ga_5Fe_3Ga_4$, and $FeGa_3$– – and two solid solution phases on the Fe-rich side, bcc-Fe and fcc-Fe, with an appreciable amount of solubility of Ga in bcc-Fe (47.5 at. % $\sim 900^\circ$ C). As a first approximation, the ordered phases (e.g., Fe-Ga with B2 structure, which consists of two interpenetrating simple cubic lattices) are not considered and are the focus of a separate study. The Fe-Ce phase diagram has been assessed by Su and Tedenac [16] and includes very low solubility of Ce in bcc-Fe (< 0.05 at. %) and a eutectic point at 592° C and 16.7 at. % Fe for liquid $\rightleftarrows CeFe_2 + \gamma - Ce$. There are two thermodynamically stable intermetallic phases $CeFe_2$ and Ce_2Fe_{17} modeled as stoichiometric compounds. The Ce-Ga phase diagram was assessed by Liu *et al.* [17] and includes four solution phases (liquid, bcc-Ce, fcc-Ce,

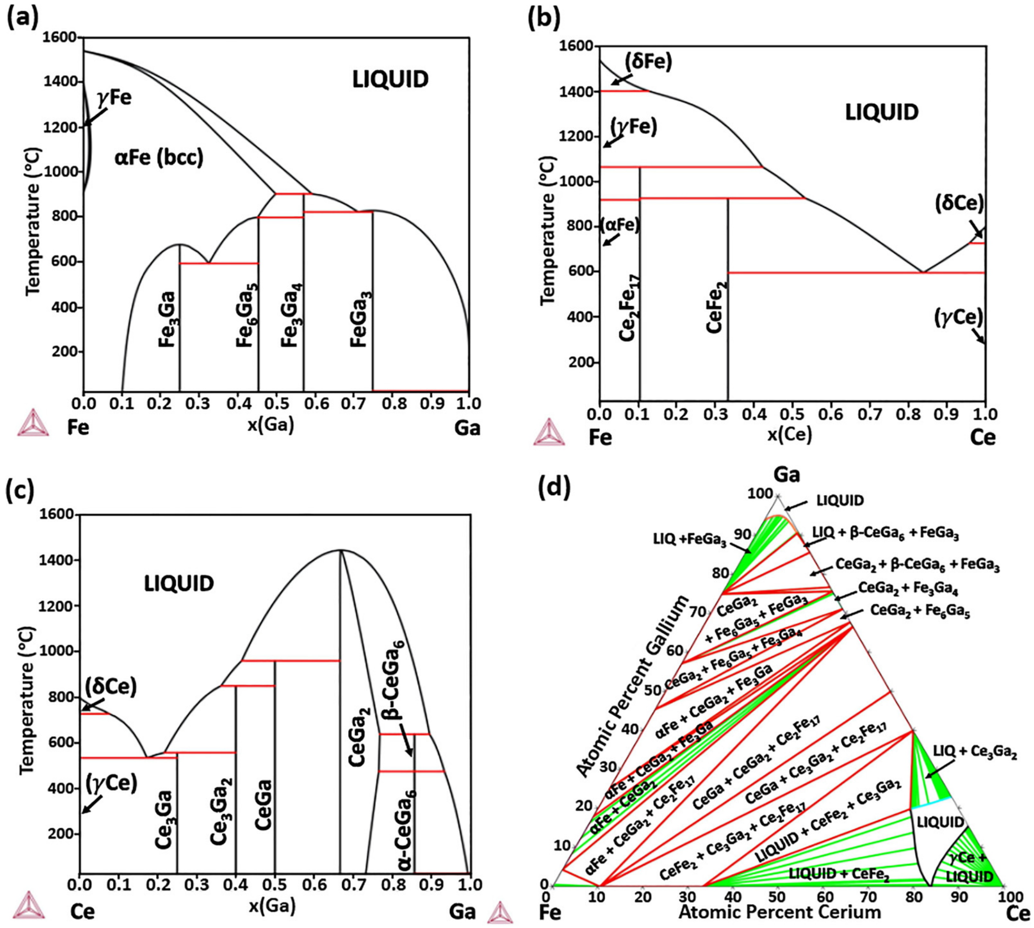

FIG. 1. (a)–(c) Calculated binary phase diagrams extrapolate to (d) Fe-Ga-Ce at 597° C. Green lines in (d) are tie lines, marking the compositions of phases that exist in equilibrium with each other at this temperature, and are only present in the two-phase region.

and orthorhombic-Ga) and five intermetallics, where Ce_3Ga, Ce_3Ga_2, CeGa, and $CeGa_6$ (α and β allotropes) are modeled as stoichiometric compounds and $CeGa_2$ is modeled with a two-sublattice model to include the hyperstoichiometric homogeneity range (antisite defect on the Ce sublattice). The three CALPHAD assessments of the binary systems (Fig. 1) are combined in a self-consistent database to explore phase stability in the ternary composition space. An extrapolation in the ternary phase space based on the binary interaction parameters at 597° C (i.e., isotherm) is presented in Fig. 1. Experimental data for the ternary phase diagram exist at 597° C by Lapunova *et al.* [18], who reported two ternary intermetallic compounds: $\tau_1 = CeFe_5Ga_7$ and $\tau_2 = CeFe_2Ga_8$, both of which are out of the composition and phase equilibria ranges studied here and are therefore not included in this paper. While some discrepancies exist between the extrapolated phase diagram and experimental findings, the computed phase boundaries within the intended composition range of this paper [$(Fe_{100-x}Ga_x)_{100-y}Ce_y$ with $15 < x < 20$ and $y < 1$] agree well with experimentally drawn phase boundaries and is sufficient for our analysis.

The CALPHAD method was used to compute the relevant phases present in the ternary Fe-Ga-Ce system with nominal alloy compositions of $(Fe_{100-x}Ga_x)_{100-y}Ce_y$ for $15 < x < 20$ and $y \leqslant 1$. The selected Fe compositions were 80, 82.5, and 85 at. %. Initial Ce doping of 1 at. % indicated formation of a $CeGa_2$ phase consuming most of the Ce and significant amounts of Ga, reducing the gallium content in the bcc-(Fe-Ga) matrix by 7–11 at. %. Alloys of composition $(Fe_{81.7}Ga_{18.3})_{100-y}Ce_y$ were chosen to account for some potential Ga loss in the bcc matrix while maintaining a specific matrix composition at $Fe_{81.7}Ga_{18.3}$, near the peak of magnetostriction [19,20]. Cerium solubility was probed as a function of composition ($0.001 < y < 1$) indicating a maximum solubility of ∼ 50 ppm, independent of Ga content. The evolution of the equilibrium phase fractions and Ce solubility in the bcc phases is reported in Fig. 2 for the $Fe_{81.696}Ga_{18.299}Ce_{0.005}$ alloy. The maximum solubility of Ce in Fe (bcc) occurs ∼ 1200° C, which was chosen as the annealing temperature for these alloys. Below 1200° C, the formation of $CeGa_2$ is dominant [Fig. 2(a)], consuming the Ce additions, where Ce content decreases in Fe (bcc) with decreasing temperature as indicated in Fig. 2(b).

Simply adding Ce to one composition therefore simultaneously changes two important variables for magnetostriction (Ce and Ga contents in the bcc matrix). To isolate the effect of Ce content on magnetostriction, the overall Ga concentration was adjusted to keep the bcc matrix at a constant composition. This matrix composition was fixed as 18.35 at. % Ga based on prior experimental results. The calculation for appropriate Ga content at a given Ce level consists of a linear interpolation between two alloys, one at the maximum solid solubility of

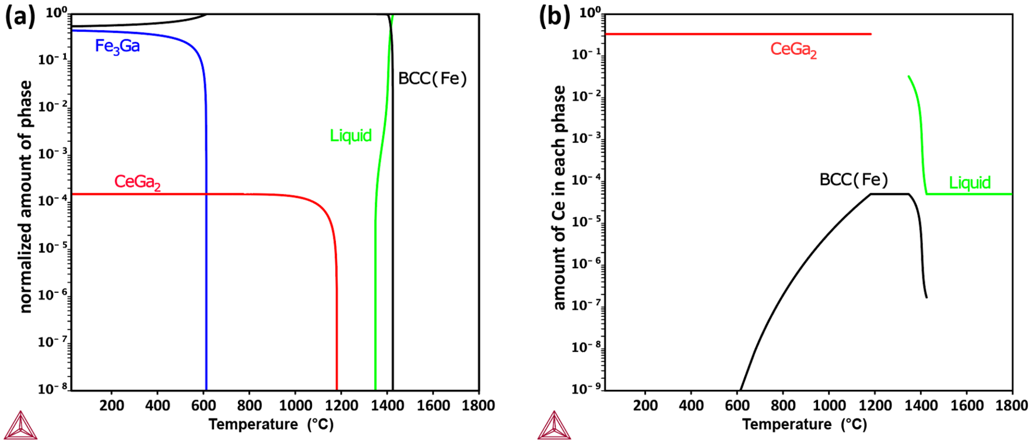

FIG. 2. Calculated (a) phase fraction and (b) fraction of Ce in each phase as a function of temperature for $Fe_{81.696}Ga_{18.299}Ce_{0.005}$, demonstrating the propensity of Ce to form $CeGa_2$ rather than entering the body-centered cubic (bcc) Fe-Ga phase. This can be mitigated by heating to 1200° C followed by a rapid quench. At higher Ce contents, the composition of the matrix phase must be adjusted to account for Ga that is pulled into the $CeGa_2$.

Ce in Fe-Ga (calculated to be 0.005 at. % Ce or 50 ppm at 1200° C) and one at an arbitrary upper limit for Ce, 1 at. % or 10 000 ppm. The overall Fe : Ga ratio of each alloy was iterated until the matrix composition was 18.35 at. % Ga. The alloys found by this method are $Fe_{81.645}Ga_{18.350}Ce_{0.005}$ and $Fe_{79.200}Ga_{19.800}Ce_{1.000}$ (in at. %). Compensated compositions were obtained by a linear interpolation between these two endpoint alloys. Table I lists compositions and relevant phase content for the endpoint alloys and interpolated alloys of interest in this paper.

IV. RESULTS AND DISCUSSION

The magnetostriction as a function of angle between strain gauge axis and applied field is presented in Fig. 3(a) for select as-melted samples, demonstrating the sinusoidal response as the sample contracts or expands relative to the sensitivity direction of the strain gauge while it is rotated with respect to the (fixed orientation) applied field of 5 kOe. Addition of as little as 65 ppm Ce leads to a more than twofold increase in response when the field is perpendicular to the strain gauge compared with pure Fe-Ga, a remarkable increase for such a dilute doping level. Increasing Ce content past this point causes maximum magnetostriction to decrease, and at 10 260 ppm, the value is comparable with that of the undoped sample. This suggests that formation of other Ce-bearing phases, such as $CeGa_2$, is actively detrimental to the magnetostrictive performance of the host lattice, a phenomenon that has previously been observed in melt-spun Fe-Ga doped with La, Er, or Dy [3,6,8].

A similar trend is observed in Fig. 3(b), which shows magnetostriction as a function of field strength, with the strain gauge aligned parallel and perpendicular to the applied field. Low levels of Ce again significantly increase the magnetostrictive response but notably also decrease the saturation field required to achieve the maximum magnetostriction, an important gain for application spaces. The 65-ppm sample showed the lowest saturation field in magnetostriction of all compositions, which could be attributed to a reduced grain size with Ce addition before the formation of $CeGa_2$, as well as demagnetization effects which are significant in magnetically soft materials such as Fe-Ga. Increasing Ce levels >150 ppm erodes this benefit too, though the effect is not as pronounced as the drop in maximum magnetostriction. The full range of magnetostriction (length change for a 90° rotation of applied field) is plotted in Fig. 3(c), displaying a peak in magnetostriction in the 65–155-ppm Ce range. Samples were also subject to a 4 h solutionizing heat treatment at 1200° C, followed by a water quench, to maximize Ce solubility into the bcc-(Fe-Ga) matrix phase and thereby increase magnetostriction. While this is not comparable with the rapid cooling achieved though nonequilibrium synthesis techniques such as melt spinning, it does lead to some gains in magnetostriction, most notably between the pure binary and 65-ppm samples, which reach relative length changes of 120 and 170 ppm, respectively. At higher Ce contents, the

TABLE I. Alloy composition in this paper. Fe and Ga content are adjusted as a function of Ce doping to keep the Ga concentration in the bcc solid solution constant at ∼ 18.35 at. %.

	Alloy composition (at. %)			Distribution of Ce and Ga (at. %)			
Target Ce doping (ppm)	Ce	Fe	Ga	Ce in bcc solid solution	Ce in $CeGa_2$	Ga in $CeGa_2$	Ga in bcc solid solution
50	0.005	81.645	18.350	0.005	0.000	0.000	18.351
200	0.020	81.608	18.372	0.005	0.015	0.030	18.351
1000	0.100	81.412	18.488	0.005	0.095	0.190	18.352
10 000	1.000	79.200	19.800	0.005	0.995	1.990	18.359

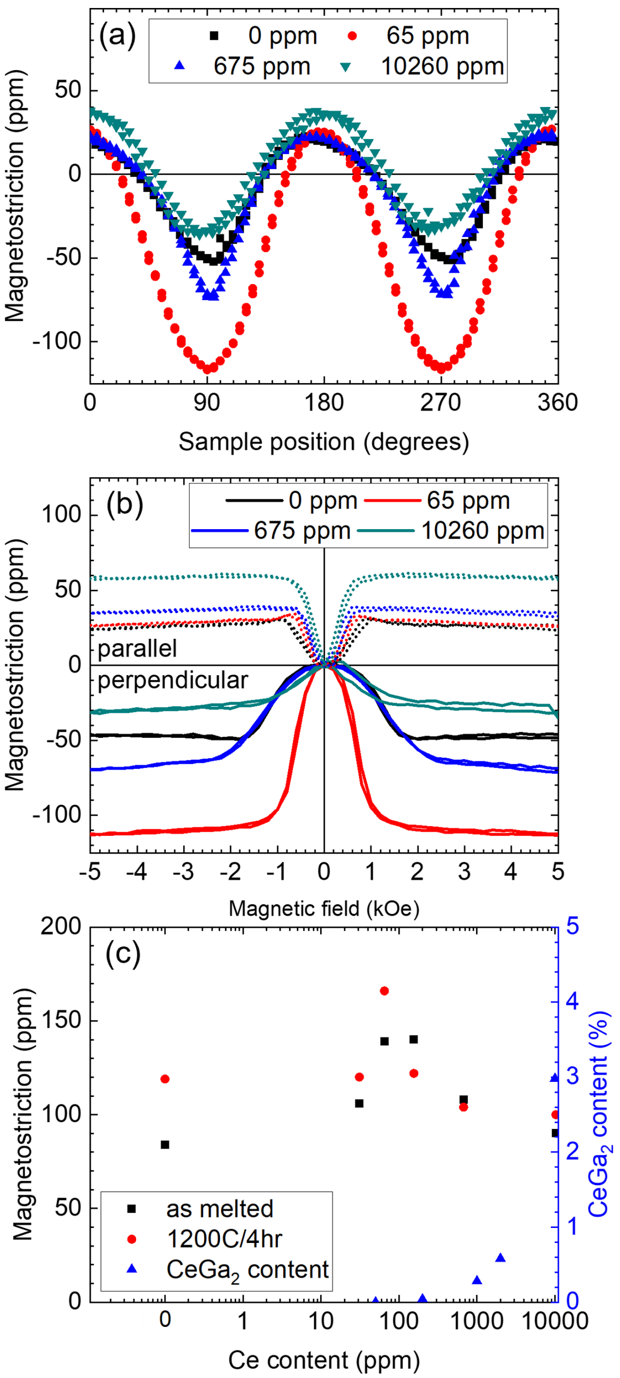

FIG. 3. (a) Magnetostriction for $Fe_{81.7}Ga_{18.3}$ samples with varying Ce concentrations at 300 K for as-melted samples in an applied field of 5 kOe as a function of angle between field and strain. Two data points are present at each angle to denote forward and backward sweeps; in most cases, these overlay, but some hysteresis is visible due to mechanical issues in the rotator. (b) Magnetostriction as a function of field in the cardinal directions, showing that, in addition to 65-ppm Ce having the largest response, it also displays the lowest saturation field. (c) Maximum magnetostriction (peak parallel minus peak perpendicular) for as-melted and heat-treated samples, showing a peak in magnetostrictive response around the solubility limit of Ce in Fe-Ga. Overdoping causes magnetostriction to decrease to levels like the binary alloy. Right axis indicates the calculated $CeGa_2$ phase fraction, showing sharp increase in nonmagnetic phase content at higher Ce levels.

heat treatment has minimal or even detrimental effect, indicating that it is not possible to dissolve the $CeGa_2$ back into binary Fe-Ga—a finding in agreement with thermodynamic calculations and corroborated by electron microscopy (see below). Magnetometry measurements did not show an evolution of saturation magnetization as a function of Ce content, as expected for such dilute concentrations. The coercivity of rectangular prisms cut from the ingots was close to identical, within error of the superconducting magnet.

Surface-sensitive XAS and XMCD measurements were conducted using TEY to assess the local coordination and magnetic character of Fe and Ce across the doping series, with results shown in Fig. 4. Despite careful handling in a glovebox and polishing immediately before loading into the vacuum system of the beamline, Fig. 4(a) displays evidence of limited surface oxidation, present as the high-energy shoulder on the L_3 peak at 708.5 eV. Since TEY probes to a depth of ~ 5 nm at the Fe $L_{2,3}$ edges, the layer thickness can be estimated as ~ 2 nm, based on relative intensity of the oxide (708.5 eV) and metallic (707 eV) peaks. The oxide layer appears slightly thinner in the undoped Fe-Ga sample; otherwise, no changes are observed in the character of the Fe XAS as a function of Ce content, as expected for such dilute concentrations. The XMCD shows slight evidence of variation, with a slight increase in spectral weight on the high side of the L_3 edge, ~ 708 eV. This contributes to the area of the L_3 edge increasing slightly for 65-ppm Ce, which can be an indication of an increase of the relative contribution of orbital angular momentum to the total magnetic moment. Similar effects have been observed for doping of Dy into pure Fe [21], though it is unclear that this would correlate with enhanced magnetostriction or the lattice contraction observed below. The presence of the surface oxide precludes straightforward application of the magneto-optical sum rules [22,23] to unambiguously determine the spin and orbital contributions to total magnetic moments.

Examination of the Ce $M_{4,5}$ edges [Fig. 4(c)] does not show evidence of oxidation, perhaps due to increased probing depth of dilute samples reducing the importance of the near-surface region. Rather, the Ce lineshape is unchanged across doping level (aside from a significant increase to a parabolic background due to the extremely weak signal at 65 ppm, which renders conventional step-edge normalization impossible), showing that Ce entering the Fe-Ga host lattice and forming $CeGa_2$ has the same valence and essentially the same coordination: Ce(III), analogous to CeF_3 [24,25] or CeCuSi [26]. A counterpart to the inflection observed in magnetostriction past 155-ppm Ce is not observed in any of the spectroscopic measurements, providing further evidence that the change in magnetostrictive response is driven by a structural change rather than an electronic one.

Lattice parameters extracted from x-ray powder patterns (Fig. 5) show a gradual contraction up to the solubility limit of Ce in Fe-Ga, which accords with previous studies [7]. The minority $CeGa_2$ phase is below the detection limit in these measurements. In common with previous work on Ce doping in Fe-Ga, the addition of Ce causes a slight contraction in the lattice. Notably, the point of maximum lattice contraction is at 65-ppm Ce, which coincides with the highest magnetostriction. This is in line with reports which found that maximizing

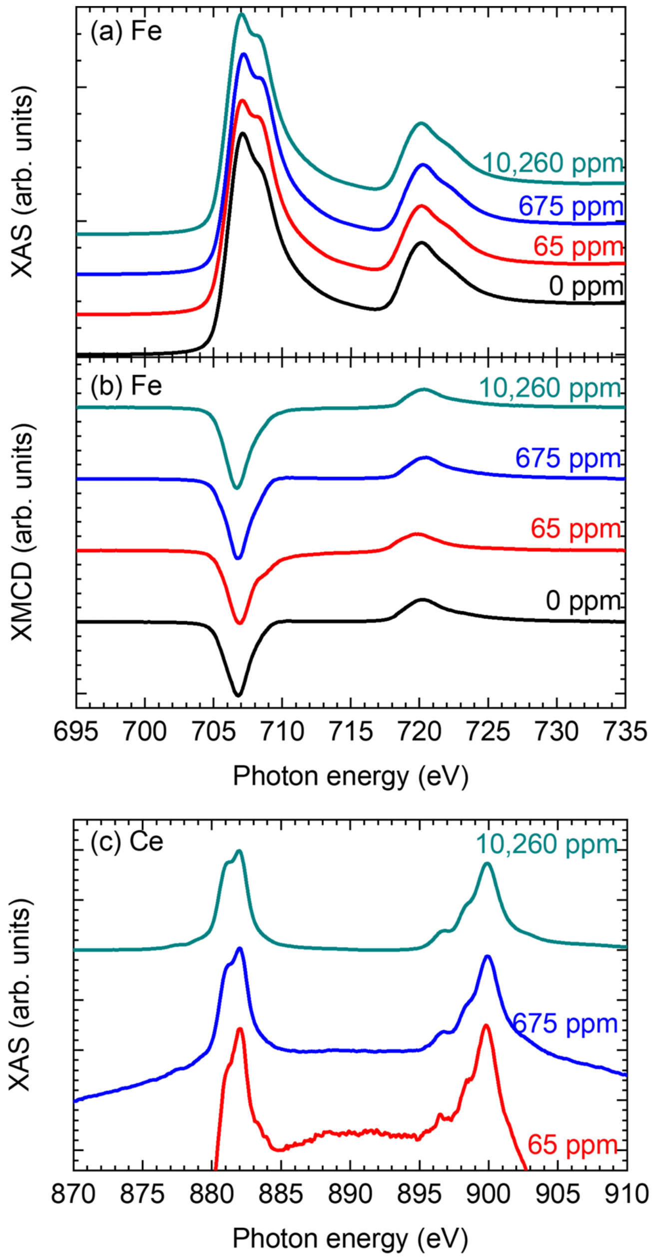

FIG. 4. (a) X-ray absorption spectroscopy (XAS) and (b) x-ray magnetic circular dichroism (XMCD) spectra gathered in surface-sensitive total electron yield mode for the Fe $L_{3,2}$ edges as a function of Ce content. No significant change in spectral shape is observed across the series, although there is some evidence for decreased surface oxidation of Fe in the Ce-free sample (reduced intensity of peak at 708.5 eV). (c) Ce $M_{4,5}$ XAS shows similarly consistent character as a function of Ce content, with Ce(III) dominating the spectrum. The low levels of Ce present in the samples lead to a large parabolic background that cannot be entirely removed and renders straightforward step-edge normalization impossible.

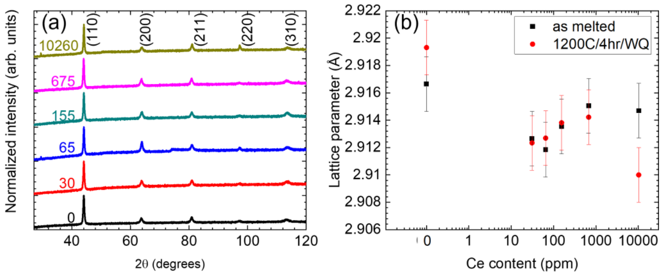

FIG. 5. (a) X-ray diffractograms for as-melted $Fe_{81.3}Ga_{18.7}$ as a function of Ce content, displaying peaks characteristic of polycrystalline body-centered cubic (bcc)-(Fe-Ga). Extracted lattice parameters are plotted in (b), where addition of Ce initially leads to a contraction of the lattice before a slight expansion is observed at higher doping levels, likely due to the formation of $CeGa_2$ (though phase fractions are below the detection limit in x-ray diffraction). Heat treatment has a significant effect on the sample without Ce, but the effects are rather smaller in Ce-bearing samples.

lattice distortions maximizes magnetostriction [3,8]; however, in these cases, the dopants lead to an expansion in the lattice. The contraction of the lattice with Ce presence is unexpected in a conventional doping scenario, where the larger Ce atom would be expected to expand the host. One possible explanation for this is that Ce acts as a grain refiner, as it is observed to lead to slightly smaller grains at low Ce levels, which changes the stress state and thus lattice parameter of the FeGa. Further work is required to better understand the mechanism behind the contraction. However, in the case of all REs, overdoping leads to the lattice reverting toward the pure binary values and a concomitant decrease in magnetostriction [3,6–8]. These changes are possibly associated with the formation of secondary phases, although the presence of an inflection point remains unexplained, and the difficulty of spatially resolving such low doping levels makes it challenging to identify whether the RE content of the matrix phase stays constant or starts decreasing as the $REGa_2$ phase forms.

EBSD measurements were performed on the as-cast 65-ppm Ce sample to better analyze the grain structure and determine if a preferential orientation had developed during solidification in the arc melter. A large area EBSD map (Fig. 6) shows grains ranging in size from a few hundred microns to several millimeters in length, with some evidence of subgrains within the larger grains.

Grains near the center of the sample are substantially larger, indicating that slower cooling rates give time for significant growth to occur, with the most pronounced growth occurring perpendicular to the copper hearth, parallel to the expected cooling direction. The formation of subgrains could be related to the presence of Ce, with small local concentrations leading to disruption of the cooling front. Orientation analysis indicates partial development of a [001] texture perpendicular with the hearth, which would act to slightly enhance magnetostriction relative to a purely randomly oriented sample. The large strain gauges employed in this paper (5 × 10 mm active area) act to minimize the effects of texturing and preferential orientation that arise from such large grains. However, there is likely still some deviation from a randomly oriented polycrystal, indicating that faster cooling rates achieved through approaches such as centrifugal casting or melt spinning could be advantageous for control of grain size as well as Ce incorporation.

SEM micrographs of samples with 0-, 675-, and 10 260-ppm Ce are presented in Fig. 7, for as-melted and heat-treated states. The pure binary is characterized by equiaxed

FIG. 6. Electron backscatter diffraction (EBSD) orientation maps of as-cast Fe-Ga with 65-ppm Ce. The top of the image corresponds to the top of the sample, while the bottom is the surface nearest the hearth of the arc melter. Large grains are visible across the vertical extent of the sample, indicating significant effects of cooling direction.

grains oE $\sim 250-\mu$m diameter, which grow to 700 μm after heat treatment. At 675-ppm Ce, the formation of a dispersed bcc Fe-Ga/$CeGa_2$ eutectic microconstituent can be observed primarily along grain boundaries. EDX point scans conducted on this network confirm a 2:1 ratio of Ga : Ce, as expected. As Ce content increases to 10 260 ppm, the bcc-(Fe-Ga)/$CeGa_2$ eutectic becomes more copious and forms an interconnected interdendritic network. As samples are heat treated at 1200° C for 4 h, the eutectic network breaks up and becomes partially spheroidized while maintaining the initial spatial distribution. Surface energy is reduced in this state, but the $CeGa_2$ is not dispersed, likely due to the low solubility and mobility of Ce in Fe [10]. More of the $CeGa_2$ particles are located within grains after grain growth, which could be responsible for the apparent decrease in magnetostriction after heat treatment. Measurements on the 65- and 155-ppm Ce samples appeared substantially equivalent to the 0-ppm sample but with a slightly smaller grain size: no Ce-rich regions could be identified due to the extremely low RE content in these materials.

V. CONCLUSIONS

In this paper, we demonstrate the dramatic impact of dilute Ce doping on the structural and magnetostrictive properties of $Fe_{81.7}Ga_{18.3}$, with doping levels as low as 65 ppm leading to a >50% increase in magnetostriction. Increasing doping past the optimal composition causes formation of $CeGa_2$, which inhibits volume changes under an applied field. Solutionizing heat treatments at 1200° C further improve magnetostriction at low Ce levels but are unable to disperse the Ce-Ga intermetallics and succeed only in breaking up the network structure. These results demonstrate the importance of considering solubility limits and kinetics during synthesis as well as confirming the great promise of RE doping to enhance the performance of galfenol for technological applications.

ACKNOWLEDGMENTS

The work in this paper was performed under the auspices of the U.S. Department of Energy (DOE) by Lawrence Livermore National Laboratory under Contract No. DE-AC52-07NA27344 and was supported by the LLNL-LDRD program under Project No. 20-ERD-059. This paper used resources of the Advanced Light Source, a U.S. DOE Office of Science User Facility under Contract No. DE-AC02-05CH11231.

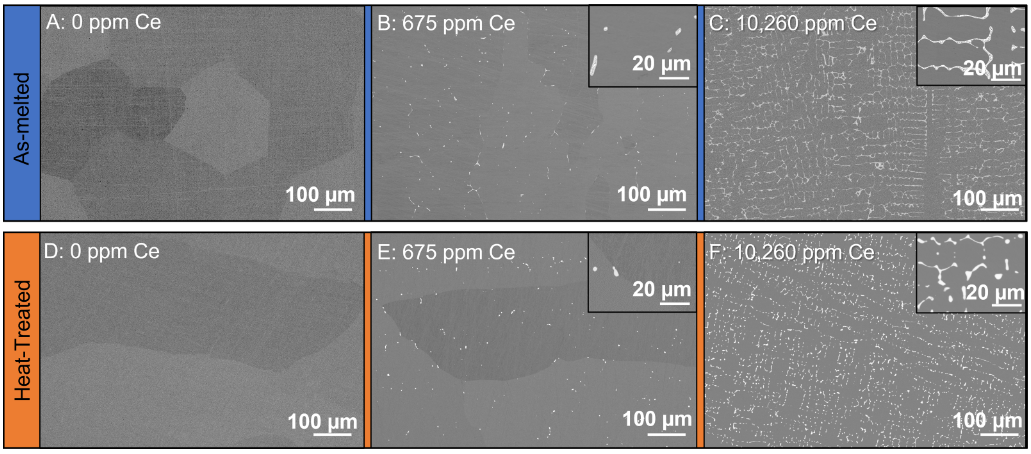

FIG. 7. (a) Scanning electron microscopy (SEM) micrographs of (a)–(c) as-melted and (d)–(f) heat-treated $Fe_{81.7}Ga_{18.3}$ with (a) and (d) 0, (b) and (e) 675, and (c) and (f) 10 260-ppm Ce. $CeGa_2$ formation is evident in the 675-ppm sample, and widespread in 10 260 ppm, where it forms a network of dendrites with regular arm spacing. Heat treatment breaks up these dendrites as particles spheroidize to reduce surface energy, but it cannot redistribute the Ce into the body-centered cubic (bcc) $Fe_{81.7}Ga_{18.3}$ matrix phase.

[1] L. D. Geng, Y. Yan, S. Priya, and Y. U. Wang, Theoretical model and computer simulation of Metglas/PZT magnetoelectric composites for voltage tunable inductor applications, Acta Mater. **140**, 97 (2017).

[2] Y. Yan, L. D. Geng, L. Zhang, X. Gao, S. Gollapudi, H.-C. Song, S. Dong, M. Sanghadasa, K. Ngo, Y. U. Wang *et al.*, Correlation between tunability and anisotropy in magnetoelectric voltage tunable inductor (VTI), Sci. Rep. **7**, 16008 (2017).

[3] Y. He, C. Jiang, W. Wu, B. Wang, H. Duan, H. Wang, T. Zhang, J. Wang, J. Liu, Z. Zhang *et al.*, Giant heterogeneous magnetostriction in Fe–Ga alloys: Effect of trace element doping, Acta Mater. **109**, 177 (2016).

[4] Y. He, X. Ke, C. Jiang, N. Miao, H. Wang, J. M. D. Coey, Y. Wang, and H. Xu, Interaction of trace rare-earth dopants and nanoheterogeneities induces giant magnetostriction in Fe-Ga alloys, Adv. Funct. Mater. **28**, 1800858 (2018).

[5] T. Jin, W. Wu, and C. Jiang, Improved magnetostriction of Dy-doped $Fe_{83}Ga_{17}$ melt-spun ribbons, Scr. Mater. **74**, 100 (2014).

[6] R. Barua, P. Taheri, Y. Chen, A. Koblischka-Veneva, M. R. Koblischka, L. Jiang, and V. G. Harris, Giant enhancement of magnetostrictive response in directionally-solidified $Fe_{83}Ga_{17}Er_x$ compounds, Materials **11**, 1039 (2018).

[7] Z. Yao, X. Tian, L. Jiang, H. Hao, G. Zhang, S. Wu, Z. Zhao, and N. Gerile, Influences of rare earth element Ce-doping and melt-spinning on microstructure and magnetostriction of $Fe_{83}Ga_{17}$ alloy, J. Alloys Compd. **637**, 431 (2015).

[8] X.-l. Wang, Y. Liu, X. Chen, H.-w. Zhang, and Y.-x. Li, Effect of Dy doping on magnetostrictive and mechanical properties of $Fe_{83}Ga_{17}$ alloy, China Foundry **17**, 198 (2020).

[9] Y. Wu, Y. Chen, C. Meng, H. Wang, X. Ke, J. Wang, J. Liu, T. Zhang, R. Yu, J. M. D. Coey *et al.*, Multiscale influence of trace Tb addition on the magnetostriction and ductility of $\langle 100 \rangle$ oriented directionally solidified Fe-Ga crystals, Phys. Rev. Mater. **3**, 033401 (2019).

[10] H. Wang, X. Gao, H. Ren, S. Chen, and Z. Yao, Diffusion coefficients of rare earth elements in fcc Fe: A first-principles study, J. Phys. Chem. Solids **112**, 153 (2018).

[11] R. M. Bozorth and R. W. Hamming, Measurement of magnetostriction in single crystals, Phys. Rev. **89**, 865 (1953).

[12] B. Sundman, H. Lukas, and S. Fries, *Computational Thermodynamics: The Calphad Method* (Cambridge University Press, Cambridge, 2007).

[13] N. Saunders and A. P. Miodownik, *CALPHAD: Calculation of Phase Diagrams): A Comprehensive Guide* (Elsevier, Oxford, 1998).

[14] L. Kaufman and H. Bernstein, *Computer Calculation of Phase Diagrams. With Special Reference to Refractory Metals, Refractory Materials. A Series of Monographs* (Academic Press Inc, New York, 1970), Vol. 4, pp. 344.

[15] E. E. Moore, P. E. A. Turchi, A. Landa, P. Söderlind, B. Oudot, J. L. Belof, S. A. Stout, and A. Perron, Development of a CALPHAD thermodynamic database for Pu-U-Fe-Ga alloys, Applied Sciences **9**, 5040 (2019).

[16] X. Su and J.-C. Tedenac, Thermodynamic modeling of the ternary Ce–Fe–Sb system: Assessment of the Ce–Sb and Ce–Fe systems, Calphad **30**, 455 (2006).

[17] J. Liu, F. Li, J. Liu, X. Zhang, T. Ahmad, and T. Liang, Thermodynamic description of the Ce–Ga and Ga–Gd systems, Monatsh. Chem. **150**, 1225 (2019).

[18] R. V. Lapunova, Yu. N. Grin', and Ya. P. Yarmolyuk, The La-Ga-Fe and Ce-Ga-Fe systems, Sov. Nonferrous Metall. Res. **2**, 116 (1983).

[19] A. E. Clark, K. B. Hathaway, M. Wun-Fogle, J. Restorff, T. A. Lograsso, V. Keppens, G. Petculescu, and R. Taylor, Extraordinary magnetoelasticity and lattice softening in bcc Fe-Ga alloys, J. Appl. Phys. **93**, 8621 (2003).

[20] R. Grossinger, R. S. Turtelli, and N. Mehmood, Magnetostriction of Fe-X (X = Al, Ga, Si, Ge) intermetallic alloys, IEEE Trans. Magn. **44**, 3001 (2008).

[21] A. A. Baker, A. I. Figueroa, G. van der Laan, and T. Hesjedal, Tailoring of magnetic properties of ultrathin epitaxial Fe films by Dy doping, AIP Advances **5**, 077117 (2015).

[22] G. van der Laan and A. I. Figueroa, X-ray magnetic circular dichroism—a versatile tool to study magnetism, Coord. Chem. Rev. **277–278**, 95 (2014).

[23] G. van der Laan, Applications of soft x-ray magnetic dichroism, J. Phys.: Conf. Ser. **430**, 012127 (2013).

[24] C. Mitra, Z. Hu, P. Raychaudhuri, S. Wirth, S. I. Csiszar, H. H. Hsieh, H. J. Lin, C. T. Chen, and L. H. Tjeng, Direct observation of electron doping in $La_{0.7}Ce_{0.3}MnO_3$ using x-ray absorption spectroscopy, Phys. Rev. B **67**, 092404 (2003).

[25] L. Howald, E. Stilp, P. D. de Réotier, A. Yaouanc, S. Raymond, C. Piamonteze, G. Lapertot, C. Baines, and H. Keller, Evidence for coexistence of bulk superconductivity and itinerant antiferromagnetism in the heavy fermion system $CeCo(In_{1-x}Cd_x)5$, Sci. Rep. **5**, 12528 (2015).

[26] J. P. Schillé, F. Bertran, M. Finazzi, C. Brouder, J. P. Kappler, and G. Krill, $4f$ orbital and spin magnetism in cerium intermetallic compounds studied by magnetic circular x-ray dichroism, Phys. Rev. B **50**, 2985 (1994).